Embedded layer of Ag nanoparticles prepared by a combined PECVD/PVD process producing SiOxCy-Ag nanocomposite thin films.

Laurent Bedel, Cyril Cayron, Michel Jouve, Francis Maury

doi:10.1088/0957-4484/23/1/015603

Embedded layer of Ag nanoparticles prepared by a combined PECVD/PVD process producing SiO_xC_y–Ag nanocomposite thin films

Laurent Bedel[1], Cyril Cayron[2], Michel Jouve[1] and Francis Maury[3]

[1] CEA, LITEN, DTNM, LTS, 17, rue des martyrs 38054 Grenoble, France
[2] CEA, LITEN, DEHT, LCPEM, Minatec, 17, rue des martyrs 38054 Grenoble, France
[3] CIRIMAT, CNRS/INPT/UPS, ENSIACET, 4 allée E Monso, BP 44362, 31030 Toulouse cedex 4, France

E-mail: laurent.bedel@cea.fr

Abstract
Structural properties of SiO_xC_y–Ag nanocomposite thin films prepared by a dual process PVD–PECVD in the same reactor have been investigated. The experimental results have demonstrated the influence of a PECVD process carried out at room temperature for the growth of a dielectric matrix on the size and the distribution density of Ag nanoparticles (NPs) deposited beforehand by magnetron sputtering. The plasma during the growth of the encapsulation SiO_xC_y layer caused a diffusion of silver from NPs through the SiO_xC_y matrix associated with a decrease in the average size of nanoparticles and an increase of their distribution density. Silver diffusion is blocked at a barrier interface to form a buried layer of individual Ag NPs which, for instance, can find plasmonic applications. Silver also diffuses toward the outer surface inducing antibacterial properties. In both cases initial Ag NPs act as reservoirs for multifunctional properties of advanced nanostructured films.

1. Introduction

Nanocomposite thin films constituted of metallic nanoparticles (NPs) embedded in a dielectric matrix are of increasing interest in many application fields such as solar cells [1, 2], sensors [3, 4] and optical devices due to their remarkable properties. The presence of nanoparticles improves light absorption due to surface plasmons [5, 6]. One of the main issues of the growth processes of these coatings is to control the nanostructuration that is essential to obtain the desired functional properties, i.e. the size, the shape and the distribution density of the metal NPs. Such films can be elaborated by vapor deposition processes [7, 8] either in one step [9, 10] or multi-step processes [11].

In one step processes, the growth of the matrix and metallic NPs occurs simultaneously and the size, the shape and the distribution density of nanoparticles depend on the process parameters. Generally, the metallic NPs are uniformly distributed throughout the thickness of the nanocomposite film. Even using a related vapor phase deposition process, the size of metallic NPs depends on the nature of the metal. Their size distribution can be monodisperse as reported for TiO_2–Ag [12] or significantly broader as for TiO_2–Cu [13]. Multi-step processes are a second route to produce nanocomposite films. Generally the architecture is based on multilayer structures. After the deposition of a controlled size and density of metal NPs, a dielectric thin film covers them. However, in this approach, the growth of the dielectric layer can affect the shape, the size and the density of nanoparticles. For instance, Simonet *et al* [11] have detected silver NPs reshaping after the growth of a Si_3N_4 encapsulation layer. The shape is also affected by the nature of the sublayer and of the top layer on Ag NPs [14].

In this work, structural properties of SiO_xC_y–Ag nanocomposite thin films prepared by a dual process in the same reactor have been investigated. The influence of the growth of the SiO_xC_y matrix deposited by plasma enhanced chemical vapor deposition (PECVD) onto Ag nanoparticles deposited by the magnetron sputtering process (physical vapor deposition, PVD) has been studied. The plasma during the growth of the encapsulation SiO_xC_y layer induces a diffusion of silver and significant changes in the average size and distribution density of Ag NPs. Nanoparticles can be pinned at a barrier interface to form a layer of individual metal NPs with a good control of their shape and their nanoscale size.

2. Experimental details

2.1. Coating deposition

The SiO_xC_y–Ag nanocomposite thin films were grown at room temperature in three steps, in the same deposition chamber, i.e. without atmospheric contamination of the samples between each step. The first and third stages consisted of the deposition of SiO_xC_y layers acting as dielectric matrix and the second one of the deposition of silver NPs. The nanostructured films were deposited on various substrates including borosilicate glass, Si wafer and copper grid with a thin film of carbon for transmission electron microscopy (TEM) direct analyses.

PECVD and PVD modules are implemented in the same reactor. The substrates are fixed on a stainless steel rotating cylindrical sample holder alternately passing in front of each depositing unit. This sequential process is adapted for the growth of multilayer nanostructures. The reactor size is approximately $90 \times 75 \times 55$ cm^3 and the diameter of the metallic sample holder is 65 cm. The two deposition modules are separated by 20 cm and the rotating speed was 1.66 cm s^{-1}. There is no heating system of the substrates and the deposition occurs at room temperature or close to it. So this reactor was also used for continuous coating on polymer supports without degradation of such thermally sensitive materials (unpublished).

The SiO_xC_y matrix was deposited by PECVD at a constant pressure of 26 Pa. A mixture of He and hexamethyldisiloxane (HMDSO) precursor (1%) was injected into the reactor as reactive gas phase. All the SiO_xC_y films were grown using low frequency plasma excitation (40 kHz) and a power density of 0.64 W cm^{-2} in a capacitive parallel plate (space 4 cm) configuration. The deposition time was fixed at 10 s. This run corresponds to one cycle and under these growth conditions the SiO_xC_y thickness is about 30 nm.

The second stage consisted of the deposition of Ag nanoparticles by pulsed magnetron sputtering at a constant pressure of about 26 Pa as well. The silver target was located at 3.5 cm distance from the substrate holder. Argon was used as sputtering gas and the power density on the silver target was fixed either at 0.7 or 1.4 W cm^{-2} depending on the number of Ag NPs required. The NPs' deposition time was fixed at 7 s and the pulse frequency was set at 100 kHz. A vacuum purge was carried out between each step to evacuate the atmosphere of the previous step using a roots pump.

In preliminary runs, the growth of SiO_xC_y/Ag/SiO_xC_y nanocomposite films was interrupted at every step, i.e. the reactor was opened between each step to wrap the silver target or the PECVD cathode in an aluminum foil to avoid possible Ag contamination during the deposition of the sandwiched dielectric layer. Because no significant difference was found with the deposition sequence described above, i.e. the steps were chained in sequence without opening the reactor to the atmosphere, this procedure was further adopted.

2.2. Characterization of thin films

The films grown on Si substrates were used to analyze the composition and the element distribution throughout the thickness of the films. X-ray photoelectron spectroscopy (XPS) was performed using a VG Escalab MKII spectrophotometer, which operated with a non-monochromatized Mg Kα source (1253.6 eV). The XPS composition profiles were determined by analyzing the surface after several Ar^+ sputtering sequences. The elements were analyzed using the core levels Si 2p, O 1s, C 1s and Ag 3d. However, the Ag 3d signal was not always detected or its intensity was too low to be extracted from the background for quantification. Secondary ion mass spectrometry (SIMS) using a CAMECA IMS 4F6 analyzer (Cs^+ bombardment) was also used to determine the element distribution throughout the film thickness with a higher depth resolution.

The size and the distribution density of Ag NPs were determined by transmission electron microscopy (TEM). The silver NPs deposited after the first and the second SiO_xC_y layer on copper grids covered by a thin carbon film were used to determine their size and the density in the same conditions as those used for the deposition onto silicon substrates. The size distribution and the densities of the silver NPs were measured with the image analysis software ImageJ. Moreover, in order to observe the distribution of silver NPs in films and to avoid possible charging effects, cross sectional samples were prepared on films grown on Si specimens. The cross-section TEM samples were prepared by mechanical tripod polishing on the MultiPrep system (Allied equipment). Ion milling and focus ion beam techniques were not used because such methods modify the Ag NPs' distribution. The TEM investigations were carried out on a conventional Jeol 2000FX TEM at 200 kV and on a probe Cs-corrected FEI Titan TEM operating at 300 kV in high resolution scanning transmission (HRSTEM) mode with bright field (BF) and in high angle annular dark field (HAADF) detectors.

The optical properties of films deposited on borosilicate glass samples were analyzed using a Perkin Elmer Lambda 950 apparatus. The transmittance was determined in the wavelength range from 200 to 800 nm.

3. Results

3.1. Size and distribution density of Ag NPs

3.1.1. TEM observations. As explained previously, films were elaborated in three steps chained successively and the expected architecture was the sandwich structure presented in

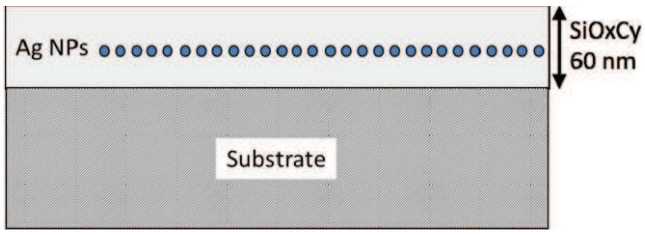

Figure 1. Expected sandwich architecture of SiO_xC_y/Ag/SiO_xC_y nanostructured thin films (total thickness 60 nm).

figure 1. Firstly, the Ag NPs size and distribution density were determined by TEM after the second stage, i.e. as-deposited Ag NPs prior to the deposition of the encapsulation SiO_xC_y layer. Figures 2(a) and 3(a) show top views of Ag NPs deposited onto a SiO_xC_y layer using a power density of 1.4 and 0.7 W cm^{-2} on the silver target, respectively. In both cases the Ag NPs are uniformly spread over the surface without coalescence. The difference of the particle size is consistent with the power density applied on the silver target during the deposition of Ag NPs. The average size decreases from 5.6 to 3.3 nm when the power density decreases from 1.4 to 0.7 W cm^{-2}.

TEM observations were also carried out after the deposition of the encapsulation SiO_xC_y layer (30 nm thick). Top views of the sandwich structure are shown for the samples prepared at 1.4 W cm^{-2} (figure 2(b)) and 0.7 W cm^{-2} (figure 3(b)). Surprisingly, this third step noticeably decreases the average size of Ag NPs from 5.6 to 3.3 nm for a power density on the silver target of 1.4 W cm^{-2} (figure 2) and from 3.3 to 1.5 nm for 0.7 W cm^{-2} (figure 3). The image analysis of figure 2 showed that the NPs density increases after the second SiO_xC_y layer deposition from 8.8×10^{11} to 1.4×10^{12} NP cm^{-2}. For both cases, the surface coverage of Ag NPs remains similar with respectively 11% and 12%. Knowing the average size and the surface density of Ag NPs and assuming that the particles are spherical, the amount of deposited silver can be estimated. The calculated Ag mass decreases from 0.42 μg cm^{-2} for as-deposited Ag NPs to 0.28 μg cm^{-2} after the deposition of the second SiO_xC_y layer. This means that approximately 33% of the silver is not quantified by this method after the growth of the dielectric top layer. For figure 3, the same tendency was observed but due to the smaller average size (1.5 nm) of the NPs on figure 3(b), the uncertainly on the NPs density is too large to get a significant result. Then, the deposition of the encapsulation SiO_xC_y layer has significantly affected the average size of Ag NPs.

3.1.2. Optical properties. The change of Ag NPs size after the growth of the top dielectric layer is also detected by optical transmittance when silver was deposited with the highest power density on the target in order to get a sufficient amount of metal NPs. For the lowest value of the power density

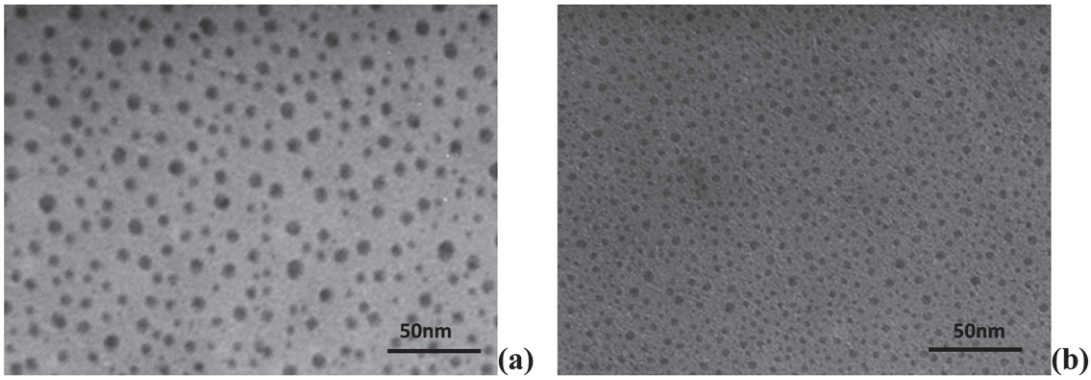

Figure 2. TEM top view of (a) as-deposited Ag NPs grown on a SiO_xC_y underlayer using a power density of 1.4 W cm^{-2} on the silver target and (b) the sandwich structure after encapsulation of the Ag NPs with the top SiO_xC_y layer.

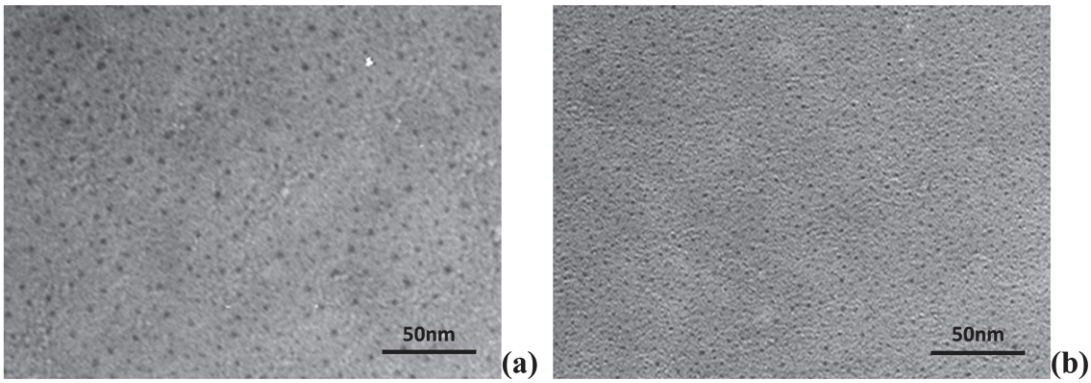

Figure 3. TEM top view of (a) as-deposited Ag NPs grown on a SiO_xC_y underlayer using a power density of 0.7 W cm^{-2} on the silver target and (b) the sandwich structure after encapsulation of the Ag NPs with the top SiO_xC_y layer.

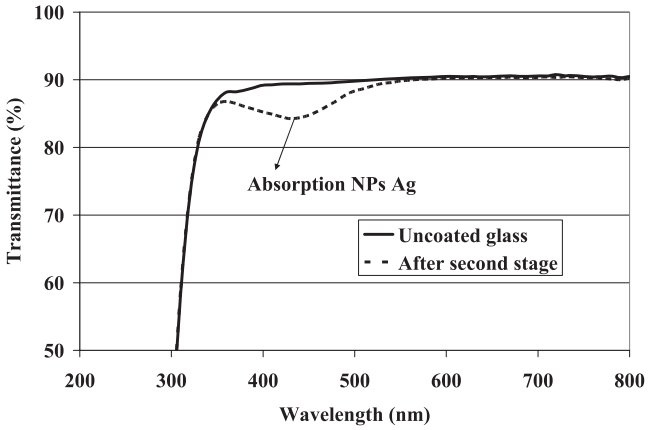

Figure 4. Transmittance spectra of a glass/SiO_xC_y/Ag sample (dotted curve) compared to that of the uncoated glass substrate (solid curve).

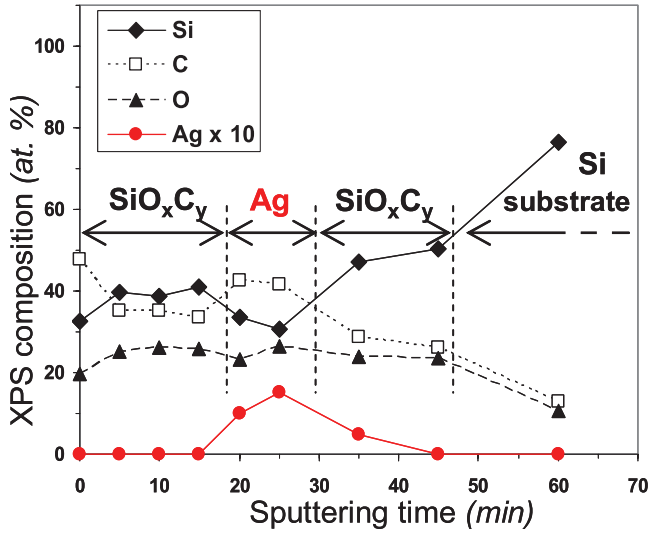

Figure 5. XPS profiles of a 60 nm thick SiO_xC_y/Ag/SiO_xC_y sample. The Ag NPs were deposited using a power density of 1.4 W cm^{-2} on the metal target.

on the Ag target the optical transmittance of a glass/SiO_xC_y/Ag sample remains similar to the one measured on an uncoated glass, i.e. 90% in the visible wavelength range and no evidence for an absorption band. By contrast, the results are different for a sample prepared with the highest power density on the Ag target. The transmittance was measured after each step (figure 4). After the first stage the optical transmittance is the same as the one measured for uncoated glass. This is consistent since the SiO_xC_y coating has a refractive index of 1.46 that is very close to the value of glass. Below 350 nm the loss of transmittance is due to the absorption of the glass substrate. After the deposition of metal NPs using a high power density on the target (second step), the presence of Ag NPs induces an absorption band which is centered at 430 nm. The deposition of the encapsulation SiO_xC_y layer causes a change in the transmittance of the sandwich sample since the adsorption centered at 430 nm disappears. Albeit the total silver content remains the same, no absorption characteristic of the metal NPs was detected and the transmittance curve is identical to the one obtained for the glass substrate or for the sample after the deposition of the first SiO_xC_y layer.

3.2. Ag depth profile through the SiO_xC_y matrix

In order to determine the real distribution of silver in the nanostructured film, XPS and SIMS analyses were conducted on SiO_xC_y (30 nm)/Ag/ SiO_xC_y (30 nm) grown on Si substrate (one cycle of deposition for each dielectric layer).

XPS profile analysis of a 60 nm thick film was sputtered during about 45 min to reach the interface with the substrate (figure 5). This multilayer profile is consistent with the growth procedure of this nanocomposite film. A maximum content of about 1.5 at.% of silver was detected in the middle of the thickness of the film prepared with a power density of 1.4 W cm^{-2}. However, the silver peak is not symmetrical since Ag is detected in the SiO_xC_y sublayer while it is not in the top one. For the films elaborated with a power density of 0.7 W cm^{-2} on the metal target, silver was not detected through the multilayer coating due to its lower content. The PECVD dielectric film grown by decomposition of HMDSO contains Si, C and O with the approximate composition $Si_{0.40}O_{0.25}C_{0.35}$. When Ag is detected, the simultaneous presence of Si, C and O in a ratio close to the dielectric layer indicates that silver does not form a continuous covering layer. This is in agreement with the fact that Ag does not wet the dielectric surface and forms metallic nanoparticles dispersed on the surface. At the depth where Ag is maximum (middle of the coating) the carbon content increases slightly from 35% to 40%. Possibly this originates from a residual contamination between the steps when the reactor is purged under vacuum to evacuate the reactive atmosphere from the PECVD step.

The SIMS analysis is more sensitive for determining composition profiles and possible diffusion of silver but the quantitative content was not determined due to the lack of reference standards. Figure 6 presents the profile of elements of the same sample as in figure 5. As for the previous figure, the interface of each layer is observed and, in addition, the native silica (SiO_2) of a few nanometers thick was clearly detected on the Si substrate, confirming the higher depth resolution of the profile SIMS analysis. On the whole, the composition profiles determined by XPS are confirmed by SIMS but these latter are more informative. First, the constant levels of Si, O and C confirm the homogeneous composition of both SiO_xC_y layers, the underlayer and the top one. The carbon enrichment at the level of the silver layer is not as clear as in XPS analysis, confirming that this variation of C content is very low. The main feature is that silver is detected all along the thickness of the nanocomposite film with an Ag peak at the expected position in the middle of the coating. The Ag distribution is not symmetrical from the middle revealing different profiles in the top and sublayer SiO_xC_y. Furthermore, a small Ag peak appears at the interface between native silica and the SiO_xC_y sublayer. The silver profile can be split in four zones. In the first one from the outer surface to the SiO_xC_y top layer/Ag interface, the intensity of Ag element increases from 2×10^2 to 2×10^3 counts s^{-1}. After that a sharp increase occurs

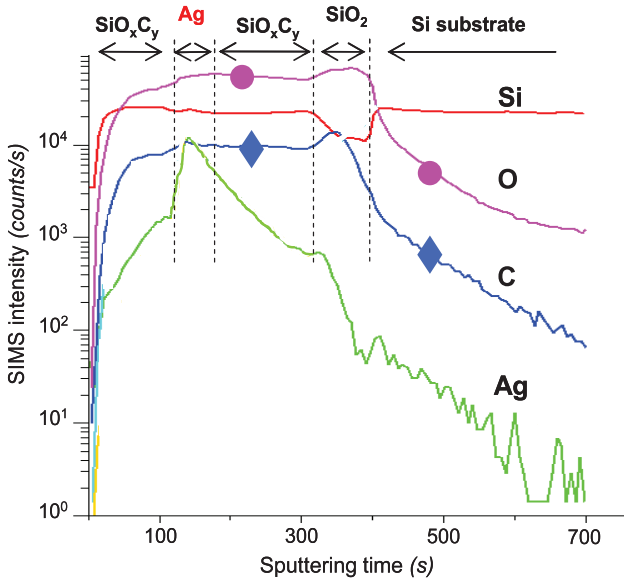

Figure 6. SIMS profiles of a SiO_xC_y (30 nm)/Ag/ SiO_xC_y (30 nm) sandwich sample obtained using Cs^+ sputtering. The encapsulation dielectric layer was grown in one cycle (30 nm thick). The different interfaces are indicated by a dotted line. The native silica layer (SiO_2) appears between the Si substrate and the first SiO_xC_y layer.

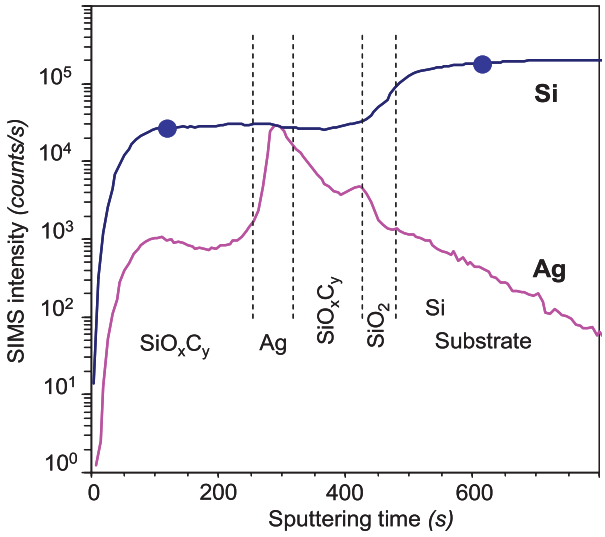

Figure 7. SIMS profiles of a SiO_xC_y (60 nm)/Ag/ SiO_xC_y (30 nm) sandwich sample obtained using Cs^+ sputtering. The encapsulation dielectric layer was grown in two cycles (60 nm thick). The different interfaces are indicated by a dotted line. The native silica layer on the Si substrate appears. Only the profiles of Si and Ag are presented for clarity.

with a maximum intensity of 10^4 counts s^{-1} in the middle of the Ag area, corresponding to the expected Ag NP layer. The third zone consists of a constant decrease of the silver intensity throughout the SiO_xC_y sublayer. The last region is the silver peak at the native silica interface. At the interface SiO_xC_y–native silica a C peak is observed as well and it could be related to the surface contamination of the substrate before the deposition of the first SiO_xC_y layer. Although the sputtering time of the two SiO_xC_y layers is not exactly the same (approximately 14% higher for the sublayer), their thickness is the same (∼30 nm). This may result from a different sputtering rate induced by the presence of Ag in the sublayer or a modification in its density after successive deposition of two other layers.

Another sample SiO_xC_y(30 nm)/Ag/SiO_xC_y (60 nm) grown on Si substrate was prepared with a 60 nm top layer of SiO_xC_y (two cycles). All other conditions remained constant. The silver profile in the SiO_xC_y sublayer is as that of the sample with the thin SiO_xC_y encapsulation layer (one cycle). This means a thicker top layer produced using two deposition cycles does not change the Ag profile in the SiO_xC_y underlayer. Despite the greater thickness of the SiO_xC_y top layer, silver is always present at the outer surface. In the 60 nm thick SiO_xC_y top layer, the silver profile is almost constant, indicating that Ag content in this top layer is likely higher than in the thinner one deposited in one cycle (figure 7). This confirms Ag is effectively present in the top layer and that the Ag signal is not an artifact due for instance to anisotropic sputtering of the sample as sometimes observed for rough interfaces. The thickness of the SiO_xC_y top layer (60 nm) is approximately 20 times larger than the average size of Ag NPs. The sputtering time to cross the SiO_xC_y top layer and Ag NP layer is not in this ratio revealing a significant difference in the sputtering rate. Consequently, the SIMS profiles were plotted versus the sputtering time rather than the thickness (figures 6 and 7).

3.3. Cross-sectional TEM observations

Cross-sectional TEM samples after the second and third stage have been observed. In the case of the complete stack Si/SiO_2/SiO_xC_y/Ag/SiO_xC_y, the TEM images in HAADF mode show (i) the presence of the expected alignment of Ag NPs between the SiO_xC_y top and sublayer (in the middle of the film), (ii) the presence of Ag NPs inside both SiO_xC_y layers and (iii), more surprisingly, a discontinuous alignment of larger Ag NPs pinned at the SiO_2/SiO_xC_y interface (figures 8 and 9). High magnifications near the SiO_2 barrier interface show the multiply twinned structure of Ag crystallites as well as the different sizes of the Ag NPs ranging from 1.3 to 9 nm (figure 9). These observations are strongly correlated with silver profiles obtained by SIMS.

TEM cross-section of as-deposited Ag NPs grown with a power density of 1.4 W cm^{-2}, i.e. a Si/SiO_2/SiO_xC_y/Ag sample, have been analyzed and no Ag NP was detected at the SiO_2/SiO_xC_y sublayer interface.

4. Discussion

In this study, the deposition of the SiO_xC_y top layer by PECVD gives evidence for a diffusion of silver from the NPs toward the two SiO_xC_y layers and essentially toward the sublayer. The average size of as-deposited Ag NPs using 1.4 W cm^{-2} of power density on the silver target was reduced by 41% after the deposition of the top layer (from 5.6 to 3.3 nm) balanced with an increase of their distribution density. This is consistent with the reduction of approximately 33% of the concentration of Ag

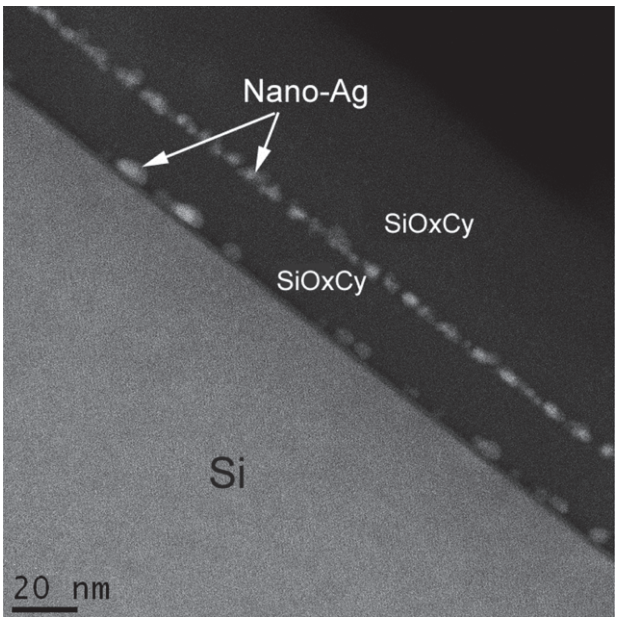

Figure 8. HRSTEM image in HAADF mode of a SiO_xC_y/Ag/SiO_x sample grown on a Si substrate with its native oxide. The Ag nanoparticles are visible in white. They are located at 30 nm from the Si substrate as expected and more surprisingly at the SiO_2/SiO_xC_y interface.

in the metal NPs (from 0.42 to 0.28 μg cm^{-2}) estimated from TEM analyses. The same tendency occurs using 0.7 W cm^{-2} of power density on the metal target. Because the solubility of Ag is negligible in SiO_2, and likely in SiO_xC_y, the silver diffusion has induced nucleation of new nanoparticles, especially at a barrier interface as SiO_2.

In the magnetron sputtering process the deposition rate increases with the power density applied on the target. As a consequence, the average size of Ag NPs was larger with a power density of 1.4 W cm^{-2} compared with 0.7 W cm^{-2}. A surface plasmon was not detected for the multilayer samples SiO_xC_y/Ag and SiO_xC_y/Ag/SiO_xC_y grown with the lowest power density applied on the target probably due to the too low size of the NPs or the low silver content in the nanostructured films. In contrast to this, by using highest power density, an absorption band centered at 430 nm was found for a SiO_xC_y/Ag bilayer sample. This band is assigned to the surface plasmon of silver in a dielectric silica layer [15, 16]. With the trilayer sample, i.e. after encapsulation with the SiO_xC_y layer, the absorption band vanished whereas the total amount of silver remains the same but silver diffusion significantly reduced the average size of NPs from 5.5 to 3.3 nm in the films. The calculation of the mass of silver detected in metal NPs from TEM top views confirms the diffusion of silver from as-deposited Ag NPs through the SiO_xC_y matrix. This decrease shows that after the deposition of the encapsulation layer all the silver is not detected by TEM as metal NPs.

As shown by SIMS analyses, the silver diffusion occurred in all the SiO_xC_y matrix. The silver profile is different in the top and the sub-SiO_xC_y layers, suggesting different transport mechanisms. For instance, Ag contamination can originate from re-sputtering metal NPs while growing the SiO_xC_y top layer or by diffusion processes. During the growth of the SiO_xC_y top layer a partial re-sputtering of silver NPs can occur by ions present in the plasma. It is well known that Ag has a sputtering rate higher than that of metals [17]. This process cannot be excluded but the fact that silver remains constant

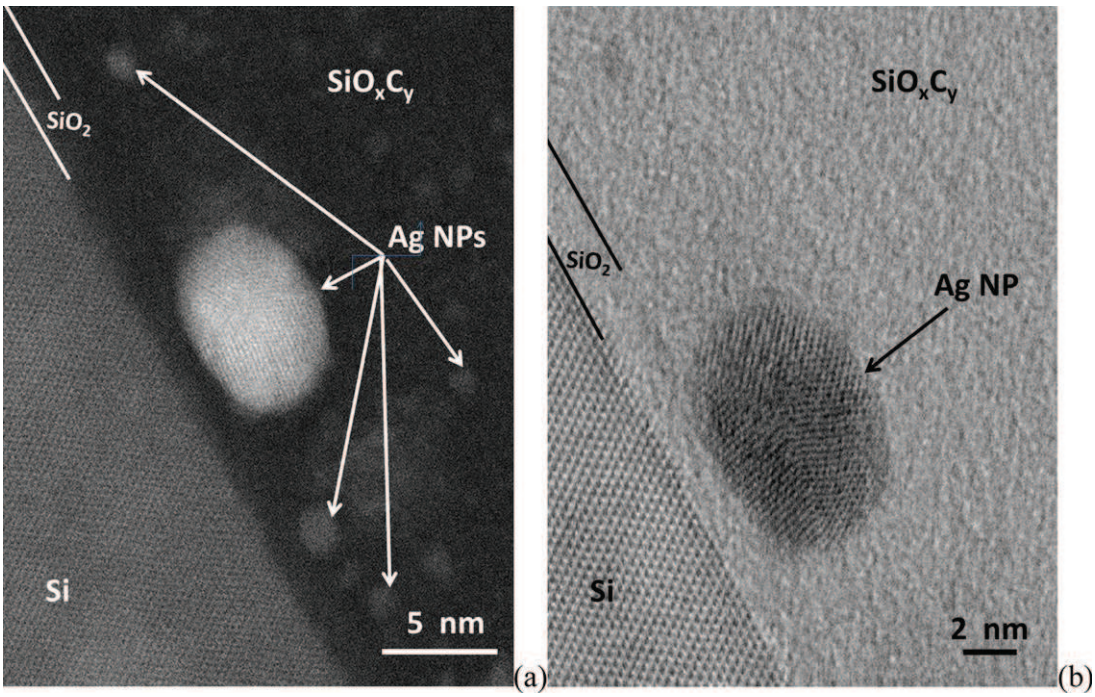

Figure 9. HRSTEM images showing (a) several small (average size 1.3 nm) and a larger (9 nm) Ag NPs blocked at the native SiO_2 layer acting as a barrier on the Si substrate and (b) the same area in bright field mode.

in the top layer of 60 nm indicates it is not the dominant mechanism because it would induce a decrease toward the outer surface (figure 7, SIMS 60 nm).

Temperature [18], electrical field [19] and photons [20] are known to be the driving force for solid diffusion. Experimental results of this work showed for SiO_xC_y–Ag nanocomposites a silver diffusion rate of at least 3 nm s^{-1}. PECVD SiO_xC_y exhibits probably a higher porosity than silica and a relatively high diffusion rate may occur. As a result, the silver readily diffused and it was blocked at the interface with the native silica layer. The enrichment of silver at this barrier layer induced a nucleation and growth of larger NPs spaced a few tens of nanometers apart (figure 8).

As the deposition time for the SiO_xC_y top layer was about 10 s, the density power applied on the PECVD cathode was as low as 0.64 W cm^{-2}, and in addition taking into account the large inertia of the rotating metal sample holder, a mechanism only activated by the temperature is excluded.

The presence of helium in the plasma generates photons in the extreme UV with high energy, as revealed by the emission spectrum of such plasma [21]. Because of the high energy of these photons, a photodiffusion mechanism could occur as previously reported for silver containing coatings [22, 23]. Then, the photodiffusion mechanism is one hypothesis in the SiO_xC_y sublayer and in the growing top layer as well.

Electromigration of metals is also a well-known diffusion mechanism as demonstrated for copper [24] and silver [25] in the electric lines of microelectronics devices. With the reactor configuration used in the present study the autopolarization of the PECVD cathode is negative and around several hundred volts [26]. As a result, the average electric field could be the dominant activation process.

Changes in the shape of silver particles during their encapsulation using several matrices were previously described [14, 27]. A diffusion of the metallic element and the nucleation of new nanoparticles were not clearly demonstrated. Toudert *et al* [15] revealed the existence of 'hidden materials' not detected by TEM in BN/Ag/BN and Si_3N_4/Ag/Si_3N_4 sandwich structures. In their case, this 'hidden material' is probably due to silver diffusion from NPs toward the dielectric matrix as demonstrated in this study for the SiO_xC_y/Ag/SiO_xC_y nanocomposite thin films.

One of these diffusion mechanisms or a combination of them could explain why silver is observed in all the SiO_xC_y matrix, especially both at a barrier layer and at the outer surface. At this stage, further specific experiments are required to clarify this transport mechanism. This result opens applications, for instance, in plasmonic (metal NP nucleation at a barrier layer) and in antibacterial surfaces (metal NPs act as antibacterial agent and as reservoir to activate the outer surface).

5. Conclusions

The experimental results have demonstrated the influence of a PECVD process carried out at room temperature for the growth of a dielectric matrix on the size and the distribution density of Ag nanoparticles deposited beforehand by magnetron sputtering. The deposition process of the encapsulation SiO_xC_y layer caused a diffusion of silver from nanoparticles through the SiO_xC_y matrix associated with a decrease in the initial size of nanoparticles and an increase in their density. The driving force of the silver diffusion comes from the plasma during the growth of the dielectric encapsulation layer. The development of such metal NPs/dielectric nanocomposite films requires a precise control of metallic nanoparticles for sensors, optical and solar applications. This work demonstrates it is possible to optimize the nanostructuration of thin films by considering the influence of the encapsulation process of metal NPs. New experiments are in progress to gain a further insight into diffusion mechanisms and results will be presented in the near future.

References

[1] Pillai S and Green M 2010 Plasmonics for photovoltaic applications *Sol. Energy Mater. Sol. Cells* **94** 1481–6

[2] Fahr S, Rockstuhl C and Lederer F 2010 Improving the efficiency of thin film tandem solar cells by plasmonic intermediate reflectors *Photon. Nanostruct.—Fundam. Appl.* **8** 291–6

[3] Wang J, Wang L, Sun Y, Zhu X, Cao Y, Wang X, Zhang H and Song D 2010 Surface plasmon resonance biosensor based on Au nanoparticle in titania sol–gel membrane *Colloids Surf.* B **75** 520–5

[4] Patskovsky S, Kabashin A V and Meunier M 2005 Near-infrared surface plasmon resonance sensing on a Si platform with nanoparticle-based signal enhancement *Opt. Mater.* **27** 1093–6

[5] Yoon W-J, Jung K, Liu J, Duraisamy T, Revur R, Teixeira F L, Sengupta S and Berger P R 2010 Plasmon-enhanced optical absorption and photocurrent in organic bulk heterojunction photovoltaic devices using self-assembled layer of silver nanoparticles *Sol. Energy Mater. Sol. Cells* **94** 128–32

[6] Akimov Yu A, Ostrikov K and Li E P 2007 Surface plasmon enhancement of optical absorption in thin-film silicon solar cells *Plasmonics* **4** 107–13

[7] Jung K H, Yoon J W, Koshizaki N and Kwon Y S 2008 Fabrication and characterization of Au/SiO_2 nanocomposite films grown by radio-frequency cosputtering *Curr. Appl. Phys.* **8** 761–5

[8] Torrell M, Cunha L, Cavaleiro A, Alves E, Barradas N P and Faz F 2010 Functional and optical properties of Au:TiO_2 nanocomposite films: the influence of thermal annealing *Appl. Surf. Sci.* **256** 6536–42

[9] Abrasonis G, Krause M, Mücklich A, Sedlackova K, Radnoczi G, Kreissig U, Kolitsch A and Möller W 2007 Growth regimes and metal enhanced 6-fold ring clustering of carbon in carbon–nickel composite thin films *Carbon* **45** 2995–3006

[10] Abe S 2011 One-step synthesis of PbSe–ZnSe composite thin film *Nanoscale Res. Lett.* **6** 324

[11] Simonet L, Babonneau D, Camelio S, Lantiat D, Guerin P, Lamongie B and Antad V 2010 *In situ* optical spectroscopy during deposition of Ag: Si_3N_4 nanocomposite films by magnetron sputtering *Thin Solid Films* **518** 2637–43

[12] Mungkalasiri J, Bedel L, Emeux F, Dore J, Renaud F N R, Sarantopoulos C and Maury F 2010 CVD elaboration of nanostructured TiO_2–Ag thin films with efficient antibacterial properties *Chem. Vapor Depos.* **16** 35–41

[13] Mungkalasiri J, Bedel L, Emeux F, Dore J, Renaud F N R and Maury F 2009 DLI–CVD of TiO_2–Cu antibacterial thin films: growth and characterization *Surf. Coat. Technol.* **204** 887–92

[14] Toudert J, Camelio S, Babonneau D, Denanot M F, Girardeau T, Espinos J P, Yubero Y and Gonzales-Elipe A R 2005 Morphology and surface-plasmon resonance of silver nanoparticles sandwiched between Si_3N_4 and BN layers *J. Appl. Phys.* **98** 114316

[15] Kobayashi Y, Katakami H, Mine E, Nagao D, Konno M and Liz-Marzán L M 2005 Silica coating of silver nanoparticles using a modified Stöber method *J. Colloid Interface Sci.* **283** 392–6

[16] Hagura N, Widiyastuti W, Iskandar F and Okuyama K 2010 Characterization of silica-coated silver nanoparticles prepared by a reverse micelle and hydrolysis–condensation process *Chem. Eng. J.* **156** 200–5

[17] Richardt A and Durand A M 1997 *Les interactions ions énergétiques-solides* (Paris: In Fine) p 19

[18] Fick J, Nicolas B, Rivero C, Elshot K, Irwin R, Richardson K A, Fischer M and Vallee R 2002 Thermally activated silver diffusion in chalcogenide thin films *Thin Solid Films* **418** 215–21

[19] Cattaruzza E, Gonella F, Ali S, Sada C and Quaranta A 2009 Silver and gold doping of SiO_2 glass by solid-state field-assisted diffusion *J. Non-Cryst. Solids* **355** 1136–9

[20] Mitkova M, Kozicki M N, Kim H C and Alford T L 2004 Thermal and photodiffusion of Ag in S-rich Ge–S amorphous films *Thin Solid Films* **449** 248–53

[21] Mills R and Ray P 2003 Extreme ultraviolet spectroscopy of helium–hydrogen plasma *J. Phys. D: Appl. Phys.* **36** 1535–42

[22] Kovalskiy A, Jain H and Mitkova M 2009 Evolution of chemical structure during silver photodiffusion into chalcogenide glass thin films *J. Non-Cryst. Solids* **355** 1924–9

[23] Mitkova M and Kozicki M N 2007 Ag-photodoping in Ge-chalcogenide amorphous thin films—reaction products and their characterization *J. Phys. Chem. Solids* **68** 866–72

[24] Meyer M A, Herrmann M, Langer E and Zschech E 2002 *In situ* SEM observation of electromigration phenomena in fully embedded copper interconnect structures *Microelectron. Eng.* **64** 375–82

[25] Hauder M *et al* 2002 Void formation and electromigration in sputtered Ag lines with different encapsulations *Sensors Actuators* A **99** 137–43

[26] Gruniger A, Bieder A, Sonnenfeld A, Rudolf von Rohr Ph, Muller U and Hauert R 2006 Influence of film structure and composition on diffusion barrier performance of SiO_x thin films deposited by PECVD *Surf. Coat. Technol.* **200** 4564–71

[27] Camelio S, Toudert J, Babonneau D and Girardeau T 2005 Tailoring of optical properties of Ag:Si_3N_4 nanocermets by changes of the cluster morphology *Appl. Phys.* B **80** 89–96